The BYU microSAR: Theory and Application of a Small, LFM-CW Synthetic Aperture Radar

Evan C. Zaugg
Brigham Young University Microwave Earth Remote Sensing Laboratory
459 Clyde Building, Provo, UT 84602 801-422-4884 zaugg@mers.byu.edu

***Abstract*— The BYU microSAR is a new, low-cost Synthetic Aperture Radar (SAR) system developed by students at Brigham Young University. The simple design is based on a linear frequency modulated continuous wave signal (LFM-CW) which reduces the size and power compared to a conventional pulsed SAR system. The BYU microSAR is small enough to fly on a small UAV, further reducing the cost of operation and extending the use of SAR into new areas. Due to the LFM-CW design, modified SAR processing algorithms are needed which account for the movement of the platform during data collection. SAR processing assumes that the sensor is moving in a straight line at a constant speed, but in actuality a UAV or airplane will deviate, often significantly, from this ideal. This non-ideal motion can seriously degrate the SAR image quality. This paper presents the design of the BYU microSAR, the theory of operation, and the modified processing algorithms which account for the continuous motion.**

I. Introduction

Synthetic Aperture Radar (SAR) has been successfully used in a variety of applications such as terrain mapping, reconnaissance, and environmental monitoring. Unfortunately, the costs associated with traditional SAR systems have precluded their use in studies requiring frequent revisits. These limitations can be overcome by using a small, low-cost, high-resolution SAR system designed for operation on a small UAV. Such a system has been developed by students at Brigham Young University [1].

Dubbed the BYU microSAR, this new system was designed based on the experience gained by previous SAR projects at BYU, e.g. [2]. The microSAR is extremely small, light-weight, low-power, and inexpensive. It was designed to fly on a UAV with a 6-foot wingspan, flying at low-altitudes ($<$ 300m), and with a limited power supply. The microSAR was designed to work within the limitations and exploit the advantages of UAV operation.

Numerous test flights have exhibited the capabilities of the microSAR system. During a flight in the Arctic, the microSAR was used to image sea ice floating in the ocean. The microSAR has also been used to image urban and rural areas in Utah. The BYU microSAR system demonstrates the utility of a low-cost, easy to operate UAV-based SAR.

Basic SAR processing assumes that the platform is moving in a straight line, at a constant speed, and with a consistent geometry with the target area. During data collection there are deviations from this ideal as the platform changes its attitude, speed, or is subjected to turbulence in the atmosphere. These displacements introduce variations in data which degrade the image quality. With the motion of the platform known, corrections can be made to the SAR data for more ideal image processing.

In traditional pulsed SAR, the platform is assumed to be stationary during each pulse and the motion takes place between pulses. With a linear frequency modulated continuous wave (LFM-CW) SAR the signal is constantly being transmitted and received, thus the motion takes place during the chirp. For motion compensation, new algorithms are needed which account for the motion during the chirp.

This paper outlines the design parameters and specifications for the BYU microSAR and discusses the implications of the design decisions. Results from microSAR data collections are also shown. The theoretical underpinnings of LFM-CW SAR and the effect of non-ideal motion are discussed and the new motion correction algorithms are developed. Simulator results are shown for correcting non-ideal motion.

The developed algorithms are applied to actual microSAR data and the results are presented. Motion data is provided by an inertial navigation system and GPS. The flight path data is interpolated between samples to provide position data for each sample of SAR data. The motion data is used to determine the necessary corrections which are introduced into the SAR data, effectively straightening the flight path.

II. BYU microSAR Design

To meet the power and cost requirements, the microSAR employs an LFM-CW signal, which maximizes the pulse length. The long pulse length allows a LFM-CW SAR to maintain a high SNR while transmitting with less peak power than pulsed SAR [3]. In a symmetric LFM-CW chirp the frequency of the signal increases from a starting frequency ω_0, and spans the bandwidth BW, at the chirp rate $k_r = BW \cdot 2 \cdot PRF$. The frequency then ramps back down as seen if Fig. 1 This up-down cycle is repeated at the pulse repetition frequency (PRF), giving a PRI of T_p. The transmitted up-chirp signal can be expressed in the time domain, where t is fast-time (the time during each pulse) and η is slow time (the time between pulses), as

$$s_t(t, \eta) = e^{j(\phi + \omega_0 t + \pi k_r t^2)}, \tag{1}$$

where ϕ is the initial phase. The down chirp is similar with $\omega_0 + BW$ being the starting frequency and $-k_r$ the chirp rate.

A simplified block diagram of the microSAR design is shown in Fig. 2. To simplify the A/D and data storage

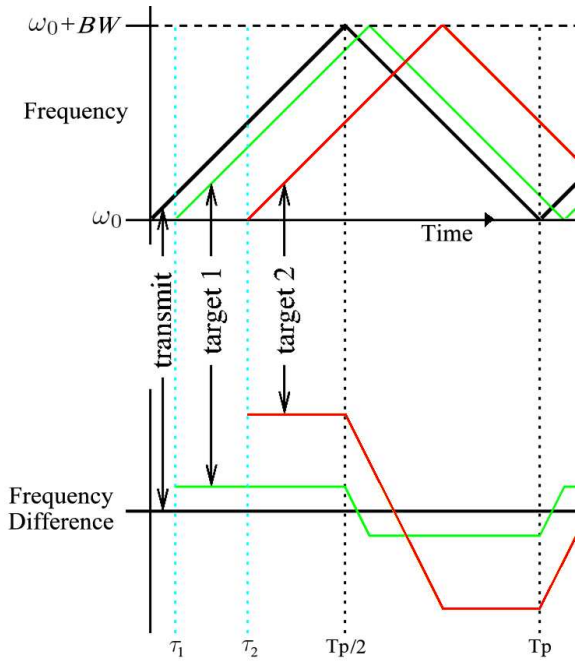

Fig. 1. The frequency change of a symmetric LFM-CW signal over time is shown above together with the signal returns from two separate targets. The frequencies of the de-chirped signal are shown below, with the times of flight, τ_1 and τ_2, due to range determining the de-chirped frequency. The relative sizes of τ_1, τ_2, and T_p are exaggerated for illustrative purposes.

hardware, the LFM-CW SAR mixes the return signal with the transmitting signal and then samples. The received signal from a target at range $R(t,\eta) = \sqrt{R_0^2 + v^2(t+\eta)^2}$, with time delay $\tau = 2R(t,\eta)/c$ is

$$s_r(t,\eta) = e^{j(\phi+\omega_0(t-\tau)+\pi k_r(t-\tau)^2)}. \quad (2)$$

The transmit signal is mixed with the received signal and low-pass filtered in hardware, which is mathematically equivalent to multiplying Eq. (1) by the complex conjugate of Eq. (2). This results in the de-chirped signal

$$s_{dc}(t,\eta) = e^{j(\omega_0\tau+2\pi k_r t\tau-\pi k_r\tau^2)}. \quad (3)$$

This simplifies the sampling hardware because the required sampling frequency is lower, although a higher dynamic sampling range is needed.

Designed to minimize size, weight, and cost, the BYU microSAR system consists of a stack of custom microstrip circuit boards measuring 3"x3.4"x4". The weight of the overall

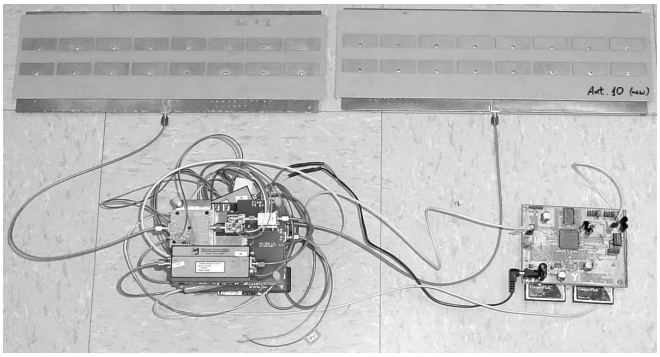

Fig. 3. Photograph of complete BYU microSAR system ready for flight on a small UAV.

system is further reduced by using no enclosure. In all it weighs less than 2 kg, including antennas and cabling.

The system architecture is divided into five subsystems which include transmit, receive, power, digital, and A/D systems. Component costs of several thousand dollars are kept low by using off-the-shelf components as much as possible.

The UAV supplies the microSAR with either +18VDC or +12VDC. The power subsystem uses standard DC/DC converters to supply the various voltages needed in the system. Power consumption during operation is nominally 18 W, with slightly more required for initial startup. The microSAR is designed for "turn-on and forget" operation. Once powered up, the system collects data continuously for up to an hour. The data are stored on-board for post-flight analysis.

The core of the system is a 100 MHz stable local oscillator (STALO). From this single source, the frequencies for operating the system are derived, including the sample clock and the radar chirp. The LFM-CW transmit chirp is digitally created using a direct digital synthesizer (DDS) which is controlled by a programmable IC microcontroller. Switches control the PRF settings, allowing it to be varied (128-2886 Hz) for flying at different heights and speeds. The programmable DDS also generates the sample clock coherent with the LFM signal.

The frequency of the LFM-CW signal is multiplied and the signal is amplified. Then it is split with one copy of the signal being mixed with the return signal and the other copy being transmitted. After amplification, the LFM-CW signal is transmitted with a power of 28 dBmW at a center frequency of 5.56 GHz and bandwidth of 80-160 MHz. The range resolution of an LFM chirp is inversely proportional to the bandwidth of

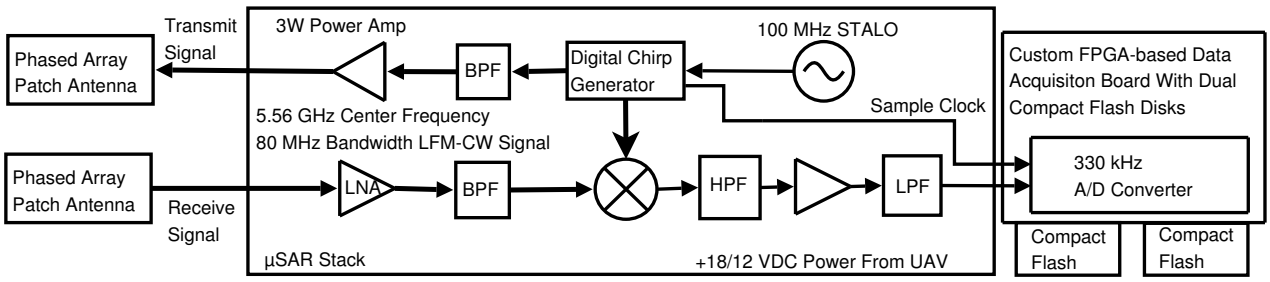

Fig. 2. Simplified BYU microSAR Block Diagram.

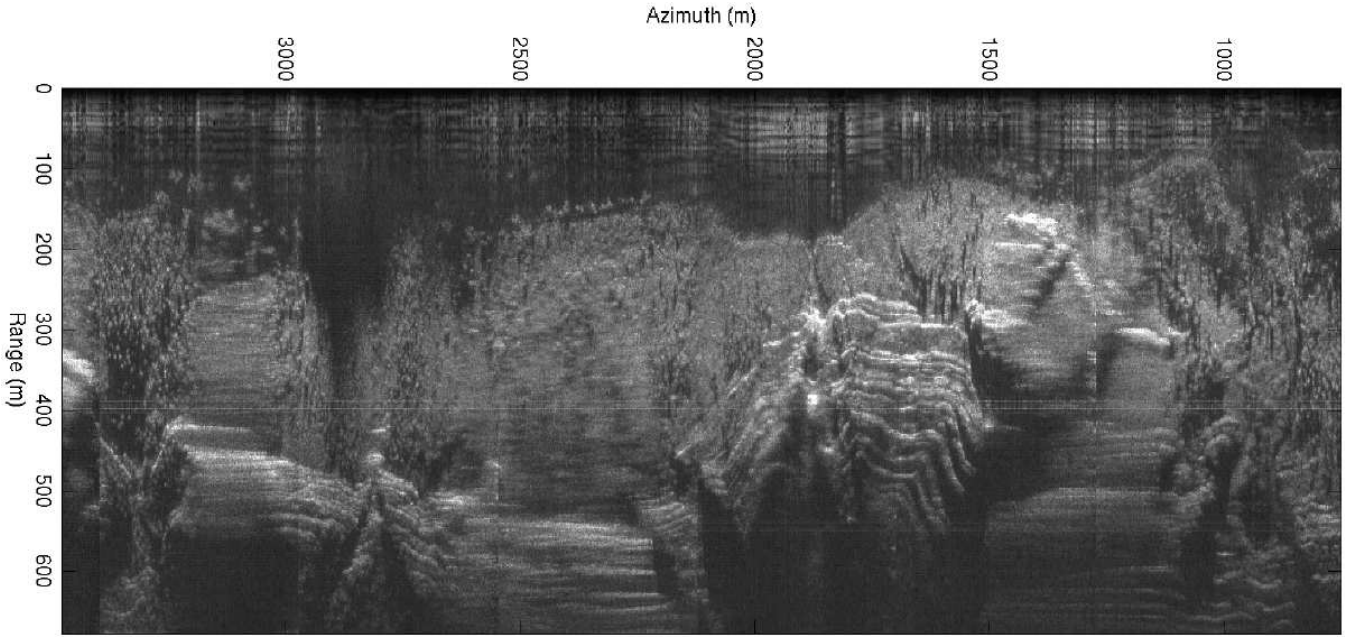

Fig. 4. Example microSAR image from a van driving up Provo Canyon, UT. Blurred sections result from the curving highway up the canyon. The canyon walls are naturally terraced and appear layered in the image.

the chirp, thus the microSAR has a range resolution of 1.875 meters at 80 MHz, and 0.9375 meters at 160 MHz.

Two identical custom microstrip antennas, each consisting of a 2x8 patch array, are used in a bi-static configuration. The antennas are constructed from coplanar printed circuit boards. A symmetric feed structure is milled on the back of one board and the patch array is milled on the front of another. The boards are sandwiched together with pins feeding the signal through the boards from the feed structure to the patches. Bi-static operation is used to maximize isolation between the transmit and receive signals. The antennas are approximately 4"x12" and have an azimuth 3dB beamwidth of 8.8° and an elevation 3dB beamwidth of 50°.

The azimuth resolution for SAR is approximately equal to half the antenna length in azimuth. This gives an azimuth resolution of 0.15 meters. In creating images from the microSAR, the data in the azimuth direction is muti-look averaged to yield a final resolution equal to the range resolution.

The return signal is amplified and mixed with the transmit signal. This de-chirped signal is filtered and then sampled with a 16 bit A/D at 328.947 kHz. A custom FPGA board was designed to sample the signal and store the data on a pair of 1GB Compact Flash disks. The data is collected continuously at a rate of 0.63 MB/second.

The microSAR can also be operated in dual-channel interferometric mode. An additional channel is created by adding another antenna and receiver board. When connected to the system, both channels are sampled, the data being interleaved and stored at a rate of 1.26 MB/second.

III. Data Processing

Processing the microSAR data is done using custom software [4]. For Range-Doppler Algorithm (RDA) processing, the signal is range compressed with an FFT in the range direction which separates the signal by frequency and thus the targets are separated in range. Then the data is taken to the range-Doppler domain with an FFT in the azimuth direction. Using standard interpolation methods the range cell migration (RCM) can be compensated and the Doppler shift introduced by the continuous motion of the platform can be removed [5].

As the SAR platform moves past a target, the phase of the return signal changes as does the range to the target. This phase-change is modeled as a frequency modulated chirp that is calculated for each range bin from the velocity of the platform, taking into account the range-walk. Azimuth compression is therefore performed by multiplying by the azimuth matched filter

$$H_{az}(f_\eta, R_0) = e^{j2\omega_0 R_0 D(f_\eta, v)/c}, \tag{4}$$

where $D(f_\eta, v) = \sqrt{1 - \lambda^2 f_\eta^2 / 4v^2}$ is the range migration factor and v is the platform along-track velocity.

Alternatively, the Frequency (or Chirp) Scaling Algorithm (FSA or CSA) [6] can also be modified to work with the de-chirped data [7]. With the FSA, the RCM and Doppler shift can be compensated without interpolation [8]. A Fourier transform is performed in the azimuth direction on the signal from Eq. (3). The resulting signal in the de-chirped-Doppler domain is

$$S(t, f_\eta) = e^{-j\frac{4\pi R_0 D(f_\eta, v)}{\lambda}} e^{-j\frac{4\pi k_r R_0 t}{cD(f_\eta, v)}} e^{j2\pi f_\eta t} e^{-j\pi k_r t^2}. \tag{5}$$

A filter is applied which removes the Doppler shift and scales the frequency.

$$H_1(t, f_\eta) = e^{-j(2\pi f_\eta t + \pi k_r t^2 (1 - D(f_\eta, v)))} \tag{6}$$

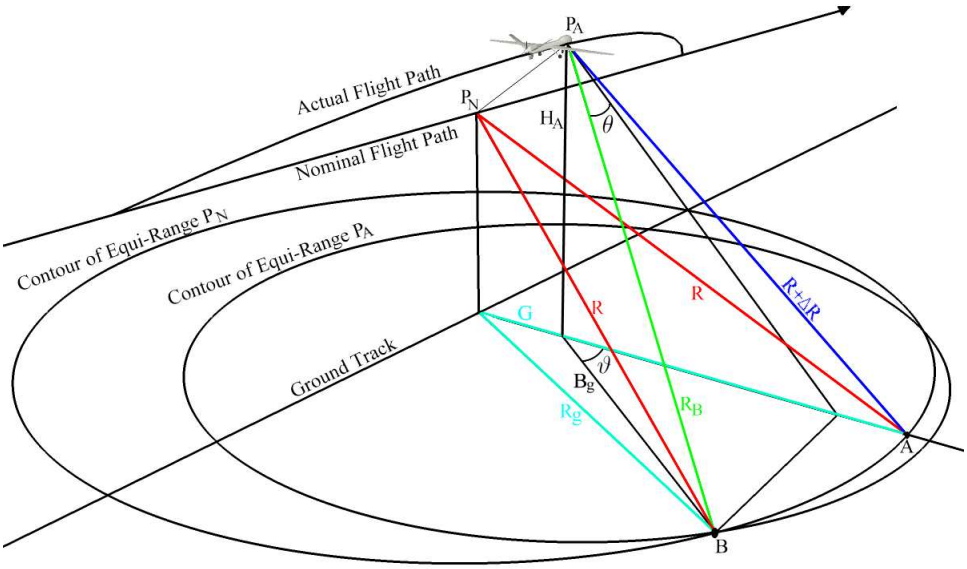

Fig. 5. The SAR platform deviates from its nominal path, point P_N, resulting in a change in range to point A from R to $R + \Delta R$. Point B is nominally at a range R, but the deviation to point P_A changes the range to R_B, which is different from ΔR.

A range FFT is performed and the second filter is applied which corrects the residual video phase.

$$H_2(f_r, f_\eta) = e^{(-j\pi f_r^2)/(k_r D(f_\eta, v))} \tag{7}$$

An inverse FFT in the range direction is performed followed by a filter that performs an inverse frequency scaling.

$$H_3(t, f_\eta) = e^{-j\pi k_r t^2 [D(f_\eta, v)^2 - D(f_\eta, v)]} \tag{8}$$

We again take the range FFT and apply the final filter that performs the azimuth compression.

$$H_4(R, f_\eta) = e^{j\frac{4\pi R}{\lambda} D(f_\eta, v)} \tag{9}$$

An azimuth IFFT results in the final focused image.

IV. Experimental Results

The microSAR system was initially tested using a ground vehicle. The antennas were mounted on the side of a van and data were collected as it drove past a variety of scenes, including urban and rural areas and a canyon. The canyon test simulates the geometry of an airborne SAR and produces images that resemble an airborne SAR image (see Fig. 4).

On 15 March 2006, the microSAR collected data while flying in a Cessna 185 over the Arctic Ocean. The images created show the structure and texture of sea ice. These were the first aerial images from the microSAR. A subsequent test flight over and area south of Provo, Utah in April of 2006 yielded images of the rural areas near Utah Lake (See Fig. 6).

The microSAR is also being tested as a stationary interferometric radar operating in differential mode to assess the possibility of detecting small shifts in mining highwalls that may be indicative of imminent failure [9]. Recent tests have been encouraging, suggesting that the microSAR is suitable for conducting further experiments to determine the limits and possibilities of using this kind of system for detecting mining hazards. Future tests would include evaluating the reliability and stability of the system while collecting data during small rock slides, simulated rain, and testing in a variety of environmental conditions.

V. Non-Ideal Motion Errors

The SAR processing algorithms described in section III assume that the platform moves at a constant speed in a straight line. In any actual data collection this is not the case, as the platform experiences a variety of deviations from the ideal path. These deviations introduce errors in the collected data which cause degradation of the SAR image.

Translational motion causes platform displacement from the nominal, ideal path, this results in the target scene changing in range during data collection. A target at range R is measured at range $R + \Delta R$ resulting in a frequency shift in the de-chirped data. The de-chirped signal in Eq. (3) then becomes

$$s_{\Delta dc}(t, \eta) = e^{-\frac{1}{2}j(\tau+\Delta\tau)(2\pi k_r \Delta\tau - 2\omega_0 - 4\pi k_r t + 2\pi k_r \tau)}. \tag{10}$$

where $\Delta\tau = 2\Delta R/c$. Targets that lie within the beamwidth that have a non-zero Doppler frequency experience a different change in range dependent on the azimuth position. This is illustrated in Fig. 5 where the range to target A changes with motion differently than the range to target B.

Variations in along-track ground speed result in non-uniform spacing of the radar pulses on the ground. This non-uniform sampling of the Doppler spectrum results in erroneous calculations of the Doppler phase history.

Changes in pitch, roll, and yaw introduce errors of a different kind. The pitching displaces the antenna footprint on the ground, the roll changes the antenna gain pattern over the target area, and the yaw introduces a squint. Pitch and yaw shift the Doppler centroid, with the shift being range dependent in the yaw case. If the Doppler spectrum is shifted so that a portion lies outside the Doppler bandwidth, then

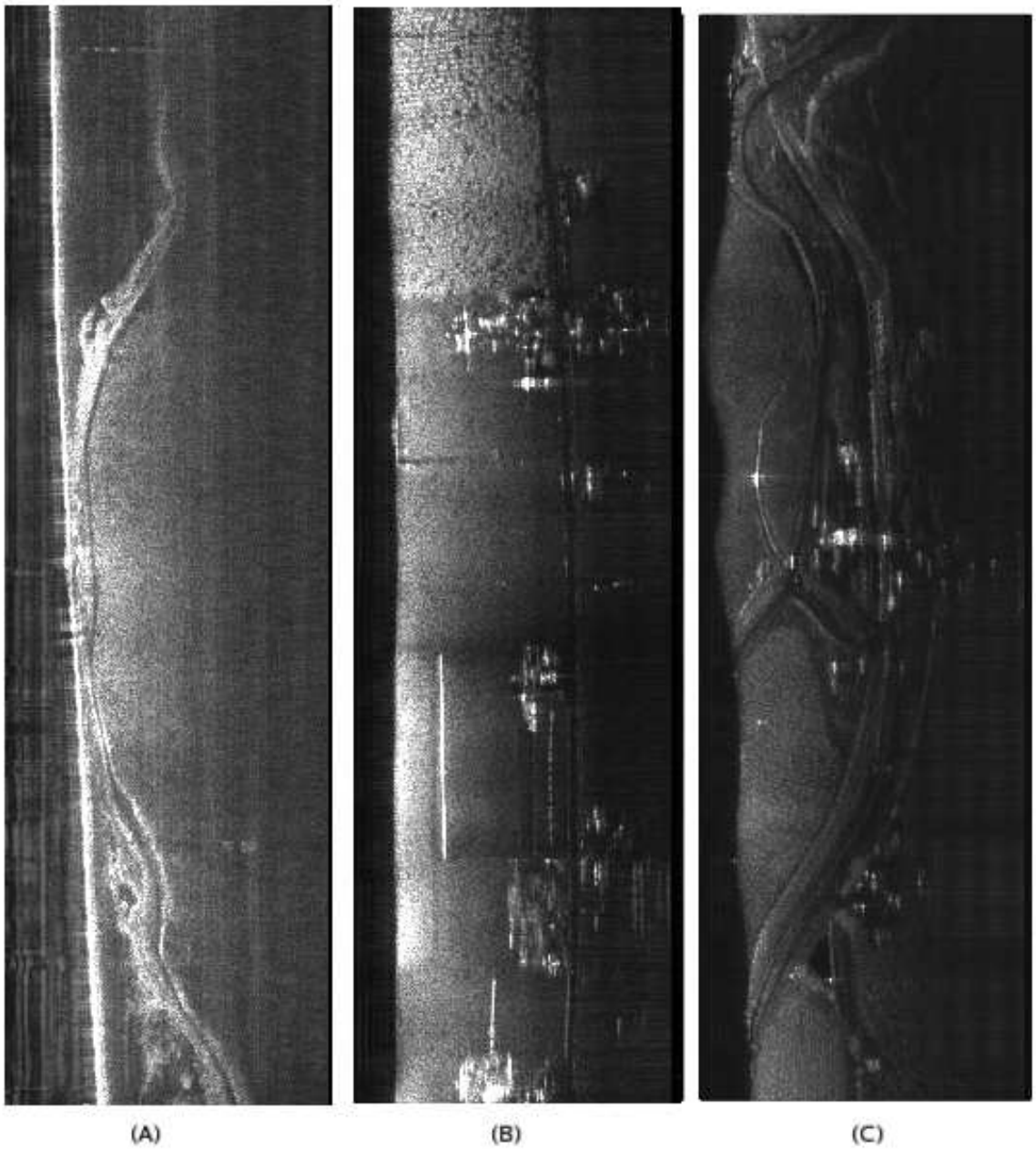

Fig. 6. Aerial microSAR images from Utah Lake and areas south of Provo, Utah. Section A shows the shoreline of Utah Lake, notice the bright nadir return from the surface of the water. Section B is an agricultural area with fields, orchards, and buildings. Section C shows a number of man-made structures that show brightly in the image.

aliasing occurs. The azimuth compression produces ghost images at the azimuth locations where the Doppler frequency is aliased to zero.

VI. Motion Compensation

Previously developed methods of motion compensation are limited for correcting the non-ideal motion of an LFM-CW SAR system. Methods like those of [10] apply a bulk motion compensation to the raw data and a secondary correction to the range compressed data. This works as an approximation for motion correction, but relies on assuming the platform is stationary during a pulse. In range compressing the data, we lose the ability to differentiate the motion over the chirp, which is problematic for LFM-CW SAR.

For an LFM-CW SAR signal, the motion corrections can be applied directly to the raw de-chirped data (Eq. 10). Doppler dependent corrections are applied to the azimuth FFT of the raw data, in the de-chirped-Doppler domain. Because each data point contains information from every range, and the corrections are range and azimuth dependent, any corrections applied in the de-chirped-Doppler domain are valid for only one single range and one azimuth value. However, with approximations these restrictions can be relaxed.

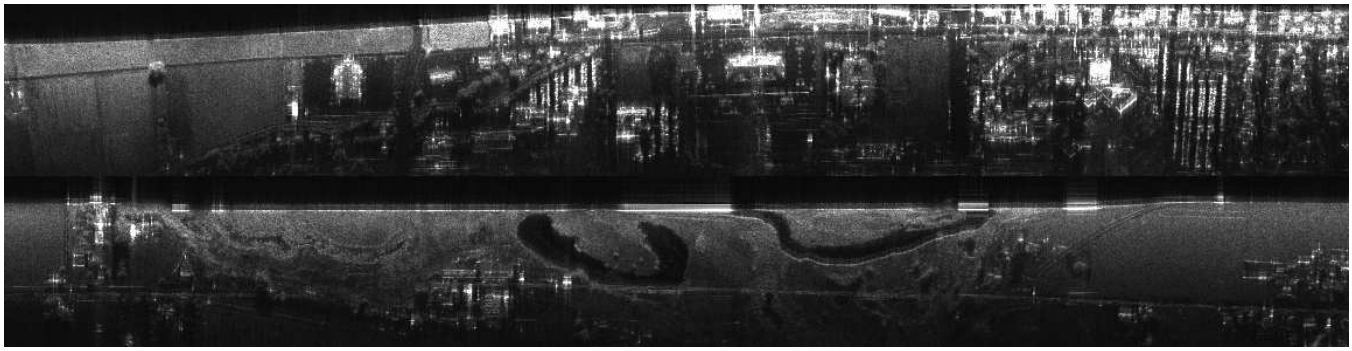

Fig. 7. A pair of microSAR images of areas near Logan, UT. The upper image shows the transition from fields to a more populated area and the lower image shows a rural area including part of a river.

A. Range Cell Migration Correction

While not a result of non-ideal motion, the RCM can be corrected without interpolation for the RDA using techniques which demonstrate the methods used for motion compensation. With the data in the de-chirped-Doppler domain, the RCM is calculated for a given range R_0 and Doppler frequency f_η

$$R_{RCM}(R_0, F_\eta, v) = R_0/D(f_\eta, v). \tag{11}$$

This range differs from our target range by $\Delta R = R_0 - R_{RCM}$ giving $\Delta\tau = 2\Delta R/c$. We apply the correction by multiplying the data in the de-chirped Doppler domain by our correction filter

$$H_{MC}(t, \Delta\tau) = e^{\frac{1}{2}j\Delta\tau(4\pi k_r\tau + 2\pi k_r\Delta\tau - 4\pi k_r - 4\pi k_r t)} \tag{12}$$

When correcting the RCM for use with the RDA, after applying the correction for a given range, R_0, an IFFT takes the data back into the time domain, an FFT performs range compression and the data in range bin R_0 is saved. The process is repeated for each value of R_0, and the composite of the corrected range bins is azimuth compressed for the final image.

B. Translational Motion Correction

In general, motion data is collected at a much slower rate than SAR data. For LFM-CW SAR the motion data must be interpolated so that every sample of SAR data has corresponding position information (as opposed to only each pulse having position data). Each data point also needs to have a corresponding location on the ideal path to which the error is corrected.

If the beamwidth is narrow then the errors due to motion can be assumed to be constant for a given range across the Doppler bandwidth. This simplifies the analysis. The flat-terrain geometry of Fig. 5 is assumed. If more precise knowledge of the terrain is available then the model can be adjusted. Knowing the coordinates of target A, the actual flight path (point P_A), and the nominal flight path (point P_N), the distances R and $R + \Delta R$ can be calculated from geometry. Again, $\Delta\tau = 2\Delta R/c$, but $\Delta\tau$ is updated for every data sample. Since we are assuming no Doppler dependence on the correction, we can apply Eq (12) directly to the raw de-chirped data. Once the corrections for a given range have been applied, processing continues using either RDA or CSA until range compression is done. As with the RCM correction formulated earlier, the correction is valid for only a single range, thus a composite range compressed image is created and then azimuth compressed to form the final image.

If the beamwidth is wide, then there are targets at the same range but different azimuth positions that experience a different range shift due to translational motion. For a given azimuth position, see Fig. 5, target B is at a position where it has the Doppler frequency f_η. The angle to target B is

$$\theta(f_\eta) = \sin^{-1}\left(\frac{f_\eta\lambda}{2v}\right). \tag{13}$$

Working through some particularly unpleasant geometry, the angle on the ground (as defined in Fig. 5) $\vartheta(\theta(f_\eta), R_g, G, H_A)$ can be found. From ϑ we can find the ground range,

$$B_g(f_\eta) = -\cos(\vartheta)G \pm \sqrt{\cos^2(\vartheta)G^2 + R_g^2 - G^2}, \tag{14}$$

and the actual range to target B,

$$R_B(f_\eta) = \sqrt{H_A^2 + B_g^2}. \tag{15}$$

We then find $\Delta R = R - R_B(f_\eta)$, $\Delta\tau = 2\Delta R(f_\eta)/c$, and apply Eq. (12) in the de-chirped-Doppler domain. This correction is valid for a single range and azimuth position and can be combined with RCM correction in a single step.

C. Velocity and Attitude

Platform velocity can also vary with time. Traditionally the data is interpolated in the azimuth direction to correct for the velocity variations across the synthetic aperture. Alternatively, the filters used in processing can be modified to match the changes in velocity.

Attitude errors generally produce negligible amounts of range displacement and principally affect the gain of the SAR image. Gain variations can usually be handled by rescaling the complex SAR image.

D. Minimizing Doppler Aliasing

Doppler aliasing occurs when the platform velocity exceeds the allowable range for a given PRF or when the pitch or yaw of the platform shifts the illuminated ground swath such that the return signal contains Doppler frequencies outside the Doppler bandwidth. A symmetric LFM-CW signal offers a

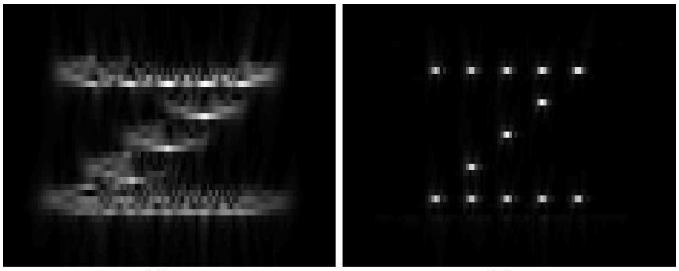

(A) (B)

Fig. 8. Simulated LFM-CW SAR data of an array of 13 point targets with non-ideal (sinusoidal translational) motion. The data is processed without motion compensation in (A) resulting in azimuth and range smearing of the targets. The same data is processed again using the motion compensation algorithms developed in this paper with the results shown in (B).

unique opportunity to minimize aliasing by exploiting the fact that for each pulse cycle there is both an up-chirp and a down-chirp which can be treated individually as successive pulses, effectively doubling the PRF. The signal for the up-chirp is given by Eqn. (1) with the recorded de-chirped signal given in Eqn. (3). The down chirp is

$$s_t(t,\eta) = e^{j\left(\phi+(\omega_0+\frac{k_r T_p}{2})(t+\frac{T_p}{2})-\pi k_r (t+\frac{T_p}{2})^2\right)}, \qquad (16)$$

with the corresponding de-chirped signal

$$s_{dc}(t,\eta) = e^{-\frac{T_p}{2} j\tau(\frac{-2\omega_0}{T_p}-\beta+\frac{4\pi\beta t}{T_p}+2\pi\beta-\frac{2\pi\beta\tau}{T_p})}. \qquad (17)$$

Which can be made to match the up-chirp by multiplying Eqn. (17) by

$$h_{du} = e^{\frac{T_p}{2} j\tau(\frac{-4\pi\beta\tau}{T_p}+\frac{4\beta t}{T_p}-\beta+2\pi\beta)} \qquad (18)$$

VII. Motion Compensation Results: Simulation and microSAR Data

An LFM-CW SAR signal from an array of point targets is simulated. Non-ideal motion is introduced into the motion of the platform, including changes in velocity, platform displacement, and attitude changes. The known deviations are used, as discussed in this paper, to correct the effects of the non-ideal motion. An example can be seen in Fig. 8.

The BYU microSAR is flown with an INS/GPS unit which measures the motion of the airplane. As discused, the motion data is interpolated and matched with the actual SAR data. The results are seen in Fig 9.

VIII. Conclusion

In this paper the design and the development of the BYU microSAR has been presented. The approach taken in designing the system to minimize size and cost has also been discussed. The successful operation of the microSAR has show the viability of a low-cost, small SAR. The use of an LFM-CW signal facilitates system miniaturization and low-power operation which make it possible to fly the microSAR on a small UAV. The ease of operation and low operating cost make it possible to make extended SAR studies of an area without a large investment and permit exploration into new applications of SAR systems.

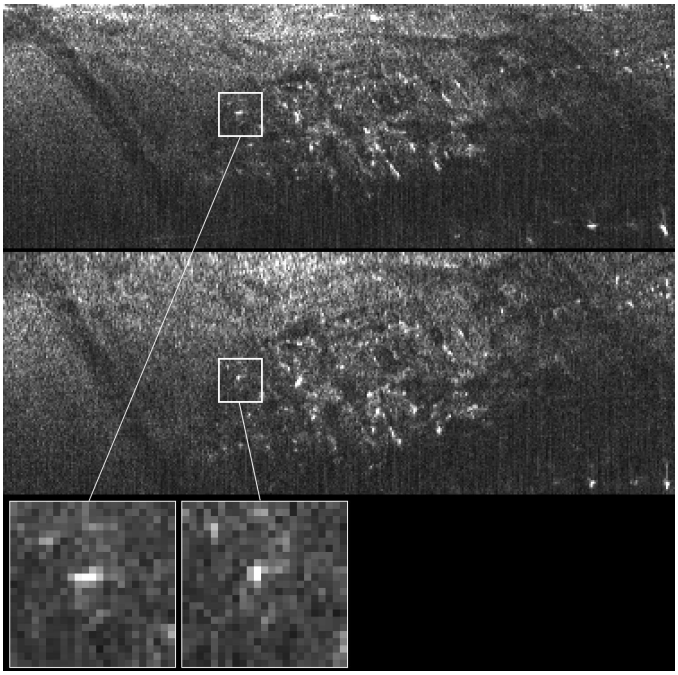

Fig. 9. The town of Newton, Utah imaged with a 160 MHz bandwidth microSAR. The top image is without motion compensation, the middle image shows the motion corrected image, and the lower images are expanded views of a point target. The motion correction improves the focusing of point targets and straightens the roads (visible on the left and right sides of the images) that were artificially curved by non-ideal motion of the airplane.

The effects of non-ideal motion on an LFM-CW SAR signal have been explored and corrective algorithms developed. The motion compensation has been successfully applied to simulated and real SAR data. With motion measurements, the negative effects of non-ideal motion can be corrected, further extending the utility of small LFM-CW SAR.

References

[1] E.C. Zaugg, D.L. Hudson, and D.G. Long, "The BYU μSAR: A Small, Student-Built SAR for UAV Operation", in *Proc. Int. Geosci. Rem. Sen. Symp.*, Denver Colorado, pp.411-414, Aug. 2006.

[2] D.G. Thompson, D.V. Arnold, and D.G. Long, "YINSAR: a Compact Low-Cost Interferometric Synthetic Aperture Radar", in *Proc. Int. Geosci. Rem. Sen. Symp.*, Hamburg, Germany, pp. 598-600, July 1999.

[3] F.T. Ulaby, R.K. Moore, and A.K. Fung, *Microwave Remote Sensing Active and Passive*, vol. 1, Artech House, 1981.

[4] M.I. Duersch, "BYU Micro-SAR: A Very Small, Low-Power, LFM-CW Synthetic Aperture Radar," Master's Thesis, Brigham Young University, Provo, Utah, 2004.

[5] J.J.M. de Wit, A. Meta, and P. Hoogeboom, "Modified range-Doppler processing for FM-CW synthetic aperture radar", in *IEEE Geoscience and Remote Sensing Letters*, vol. 3, pp. 83-87, Jan. 2006.

[6] I.G. Cumming and F.H. Wong, *Digital Processing of Synthetic Aperture Radar Data*, Artech House, 2005.

[7] J. Mittermayer, A. Moreira, and O. Loffeld, "Spotlight SAR data processing using the frequency scaling algorithm", in *IEEE Trans. Geosci. Remote Sensing*, vol. 37, pp. 2198-2214, Sept. 1999.

[8] A. Meta, P. Hoogeboom, and L.P. Ligthart, "Non-linear Frequency Scaling Algorithm for FMCW SAR Data", in *Proc. 3rd European Radar Conference, 2006*, pp. 9-12, Sept. 2006.

[9] E.L. McHugh, D.G. Long, and C. Sabine, "Applications of Ground-Based Radar to Mine Slope Monitoring", *ASPRS Annual Conf. Proc.*, Denver, Colorado, 12 p., May 23-28, 2004.

[10] A. Moreira, and Y. Huang, "Airborne SAR processing of highly squinted data using a chirp scaling approach with integrated motion compensation", in *IEEE Trans. Geosci. Remote Sensing*, vol. 32, pp. 1029-1040, Sept. 1994.